Granular element method for computational particle mechanics

José E. Andrade[*], Keng-Wit Lim, Carlos F. Avila, and Ivan Vlahinić

Division of Engineering & Applied Science, California Institute of Technology, Pasadena, CA 91125, USA

Abstract

This paper presents a method within the family of the Discrete Element Method (DEM) capable of accurately capturing grain shape by using Non-Uniform Rational Basis-Splines (NURBS). The new method, called GEM, bypasses one of the current bottlenecks in computational discrete mechanics of granular materials by allowing discrete elements to take realistic and complex granular shapes encountered in engineering and science (e.g., sand grains). More than a new method, this paper presents a new concept for DEM: using NURBS to seamlessly transition from advanced visualization tools (e.g., X-ray CT) to physics-based computational models where particle shape is realistically modeled. It is expected that, with the rapid advancement of computational power, combining high-fidelity characterization with physics-based computations will lead to more predictive modeling approaches. The granular element method may help transition from characterization to modeling and could lead to more realistic predictions at the grain scale.

Keywords: Discrete element method; particle mechanics; NURBS; multiscale analysis

---
[*]Corresponding author. E-mail: jandrade@caltech.edu (J. E. Andrade).

1   Introduction

Particle morphology can be characterized, in general, by three properties: sphericity, roundness, and roughness [1]. These properties are sometimes referred to by other names such as shape, angularity, and surface roughness, respectively [2]. In either case, these properties are scale dependent, as they measure morphological characteristics at different length scales, with increased spatial resolution needed to measure roughness, for example. Particle morphology has been shown to be crucially important for macroscopic properties in granular materials. Some of the most critical macroscopic properties used in engineering and science are strength and permeability, and both of these are intimately affected by particle morphology (see, for example, [1; 3]). In the case of macroscopic strength, it has been determined that lack of sphericity, sharper angularity and increased roughness all lead to increased mobilized strength in granular materials [1]. This macroscopic effect is due to micromechanical effects such as increased number of contact points. Therefore, accurate micromechanical models for granular materials should be able to correctly capture particle morphology if they are to correctly predict the macroscopic strength in real materials such as sands.

The Discrete Element Method (DEM) was introduced three decades ago [4] predicated on the possibility of revealing micromechanical features that were simply not accessible to continuum models. This modeling paradigm has allowed tremendous access to understand most features of the micromechanical behavior of granular materials and link them with macroscopic response [5]. However, the link to macroscopic response remains qualitative and this is mostly due to the inability to capture grain morphology accurately. Clumping [6; 7] and polyhedra [8; 9; 10; 11] are currently the two salient techniques that can be used to capture three-dimensional particle morphology in natural materials. Another class of DEM is based on superquadrics. Superquadrics are defined through an implicit function controlling the 'blockiness' of the particles and are supersets of ellipses and ellipsoids [12]. DEM based on ellipses and ellipsoids [13; 14] appears to be the most popular approach after clumping and polyhedra. Clumping is relatively simple to implement in current codes but cannot represent particle curvature readily, which could impact contact properties such as normal and tangential forces, thereby potentially changing macroscopic response. On the other hand, polyhedra can represent complex geometrical entities fairly well (especially in two dimensions), but contact detection algorithms available for these geometrical entities are rather

complex (especially in three dimensions) as they introduce the need to deal with face-to-node, node-to-node, and face-to-face contact. A new technique called 'potential particles' was introduced in [15], where a thorough state-of-the-art in DEM is presented and current bottlenecks in capturing particle morphology are highlighted.

New characterization tools such as X-ray computed tomography (CT) enable direct measurement of particle morphology, as a function of imaging resolution. Figure 1(a) shows an example of a sand particle imaged with 3D X-ray CT with thousands of voxels used to render morphology accurately (e.g., shape and angularity). In light of these advances in characterization of granular materials, and the tremendous increase in computational power, we propose a new paradigm for discrete element methods based on Non-Uniform Rational Basis-Splines (NURBS). We call this new technique the Granular Element Method (GEM) and propose its use as a significant enhancement to represent granular morphology in three dimensions directly from characterization tools and with smooth surfaces that can facilitate accurate contact calculations. Figure 1 shows the concept to seamlessly transition from an image in (a) to a smooth functional representation using NURBS in (c). The intermediate figure in (b) shows the scaffolding furnished by the so-called control points necessitated in NURBS technology. It should be noted that while GEM aims to directly capture the first two levels of geometrical morphology, such as sphericity and roundness, it will rely on the concept of an effective interparticle friction coefficient in order to account for the effect of particle roughness.
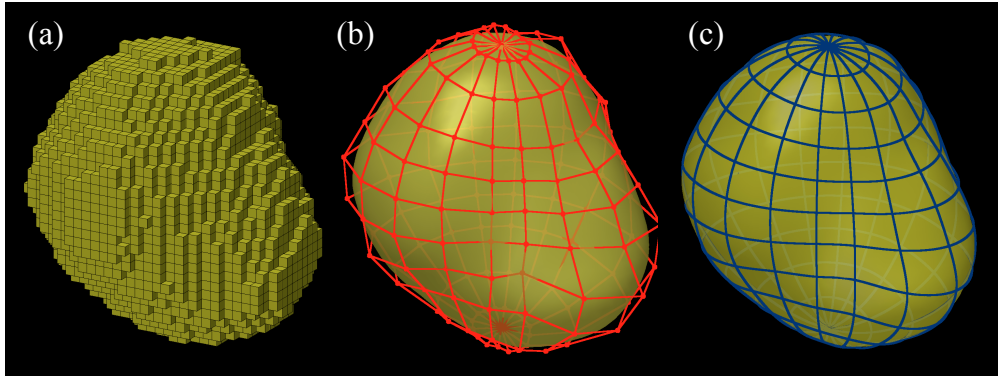

Figure 1: Proposed GEM concept using NURBS as an isoparametric representation for grain morphology and discrete element calculations.

The use of NURBS for DEM calculations within the GEM paradigm promises several significant

advantages for accuracy and efficiency in computations. NURBS are ideal functions to capture grain morphology in an unprecedented fashion. For example, the graphics industry relies on Non-Uniform Rational Basis-Splines (NURBS) to represent complex geometries in 2D and 3D and to even perform animations [16]. Also, the ability of these functions to work as bases for so-called isogeometric analysis has been demonstrated recently [17]. Based on these recent developments, we propose the use of NURBS, which are already used in visualization software (e.g., AVISO®) to render X-ray CT images, as the basis for DEM calculations. As will be shown in the paper, GEM requires minimal changes to existing DEM codes and can exploit the rapidly-improving technologies available in the computing graphics industry, for instance. This can significantly accelerate computational efficiency, which is needed for the additional computational expenses associated with contact detection in complex geometries parametrized by NURBS.

The structure of the paper is as follows. In the first section, we discuss the basic ingredients of GEM. First, we recall some basic theory of NURBS for the description of curves. Second, we summarize the basic equations of motion and the discrete update equations of GEM. Third, we present a description on the contact force calculation relevant to GEM. A section is devoted to the discussion on the computational cost of GEM. We then present two examples that showcase the capabilities of GEM. In this paper, for simplicity of presentation, we limit our discussion of GEM to two-dimensional problems, however, we note the applicability of the method to three dimensions, as depicted conceptually in Figure 1.

2 GEM: a discrete element method based on NURBS

2.1 Non-Uniform Rational Basis-Splines (NURBS)

Non-Uniform Rational Basis-Splines (NURBS) are ubiquitous in the world of computer graphics, computer-aided design (CAD), computer-aided engineering (CAE), and computer-aided manufacturing (CAM) systems, and even computer animations. These functions provide great flexibility in representing arbitrary and complex geometries with much less information than conventional faceted or polynomial counterparts. Perhaps more importantly, in the context of this work and as shown in this section, the mathematical properties of NURBS make them ideal candidates for the description of grain morphology, the integration of discrete equations of motion, and the detection

of contact.

In what follows we briefly describe the essential components of NURBS in the context of the current application. The literature on NURBS is extensive and relatively mature, and our purpose here is not to present all of its elements but rather those that are needed for completeness of presentation. For an exhaustive description of NURBS the reader is referred to [17; 18; 19; 20], whose presentation and notational convention we follow closely. For instance, in this paper, we adhere to the convention in the computational geometry literature where the degree $p = 0, 1, 2, 3$, etc. refers to constant, linear, quadratic, cubic, etc., piecewise polynomials, respectively. In the following incomplete description of NURBS, we split the acronym into three parts: Non-Uniform (NU), Rational (R), and Basis-Splines (BS), describing these parts in reverse order and incrementally for clarity of presentation.

2.1.1 Basis-Splines (BS)

Within the description of Basis-Splines (B-Splines), there are three essential elements [20]:

1. A set of $n + 1$ control points $\mathbf{P}_i$ ($0 \leq i \leq n$),

2. A knot vector U of $m + 1$ knots ($0 = u_0 \leq u_1 \leq \cdots \leq u_{m-1} \leq u_m = 1$), and

3. A degree p satisfying $m = n + o$ where $o = p + 1$ is the order of the curve.

Note that the last requirement means that the number of knots $m + 1$ must be equal to the number of control points $n + 1$ plus the curve order $p + 1$. The control points need not lie on the curve itself. Rather, control points act as a scaffold that controls the geometry [17]. At the most rudimentary level, one manipulates the geometry by adjusting the control points until the desired shape is met. Piecewise linear interpolation of the control points effectively furnishes a control polygon bounding the geometry.

Given the aforementioned paramenters, a (non-rational, polynomial) B-Spline curve is defined parametrically such that

$$\mathbf{C}(u) = \sum_{i=0}^{n} N_{i,p}(u)\, \mathbf{P}_i \tag{1}$$

where u is the curve parameter, and $N_{i,p}$ is the i-th B-Spline basis function of degree p defined recursively as follows:

$$
\begin{aligned}
N_{i,0}(u) &= \begin{cases} 1 & \text{if } u \in [u_i, u_{i+1}) \\ 0 & \text{otherwise} \end{cases} \\
N_{i,p}(u) &= \frac{u - u_i}{u_{i+p} - u_i} N_{i,p-1}(u) + \frac{u_{i+p+1} - u}{u_{i+p+1} - u_{i+p}} N_{i,p-1}(u)
\end{aligned} \tag{2}
$$

The above is also known as the Cox-de Boor recursion formula [21; 22].

2.1.2 Rational B-Splines (RBS)

A known limitation of (non-rational) B-Splines, as defined in equation (1), is their inability to capture conic sections (e.g., circles and ellipses). This limitation stems from the simple polynomial form of B-Splines. To be able to represent conic sections, the parametric form would need to be *rational*, i.e., the quotient of two polynomials. A rational B-Spline (RBS) is furnished by adding a weight $w_i \geq 0$, which provides an additional degree of freedom for geometry manipulation. Hence, the curve equation becomes

$$
\begin{aligned}
\mathbf{C}(u) &= \frac{1}{\sum_{j=0}^n N_{j,p}(u) w_j} \sum_{i=0}^n N_{i,p}(u) w_i\, \mathbf{P}_i \\
&= \sum_{i=0}^n R_{i,p}(u)\, \mathbf{P}_i
\end{aligned} \tag{3}
$$

where $R_{i,p}(u) = N_{i,p}(u)\, w_i / \left(\sum_{j=0}^n N_{j,p}(u)\, w_j \right)$, $0 \leq i \leq n$, are the rational basis functions. Since $R_{i,p}(u)$ is rational, the exact description of conic sections becomes possible. Naturally, when all weights are equal to unity, equation (3) reduces to equation (1).

It is interesting to note the geometric contribution furnished by the weights. The weight w_k affects the effective contribution of control point $\mathbf{P}_k$ on the overall shape of the curve $\mathbf{C}(u)$. Making w_k smaller corresponds to "pushing" the curve away from the control point $\mathbf{P}_k$. In the extreme, when $w_k = 0$, the term $w_k \mathbf{P}_k$ is annihilated from the equation of the curve and the contribution of the control point is obviously nullified. Another interesting extreme is obtained by making w_k

very large relative to other weights. Dividing equation (3) by w_k gives

$$\boldsymbol{C}(u) = \frac{\sum_{i \neq k}^{n} N_{i,p}(u) w_i / w_k \boldsymbol{P}_i + N_{k,p}(u) \boldsymbol{P}_k}{\sum_{i \neq k}^{n} N_{i,p}(u) w_i / w_k + N_{k,p}(u)} \tag{4}$$

where one can see that as w_k is increased, the curve $\boldsymbol{C}(u)$ is "pulled" towards the control point $\boldsymbol{P}_k$.

Remark 1. Within the context of GEM, the inability of non-rational B-Splines to represent conic sections should not be viewed as a disadvantage, since real grains are rarely spherical or circular in section. NURBS can be used in their simpler polynomial B-spline version when their full power is not necessary.

2.1.3 Non-Uniform (NU) Rational B-Splines (NURBS)

The NU portion in NURBS is furnished by the knots in the knot vector U of the B-Splines. The non-decreasing knots u_i, $i = 0, 1, ..., m$ partition the parameter space into segments of half-open intervals $[u_i, u_{i+1})$, which are also called knot spans. The knot span can be of zero length since the knots need not be distinct, i.e., they can be repeated. The number of times a knot value repeats itself is called multiplicity k. Based on the way the knots are spaced, we can divide B-Splines into the following types:

1. Uniform B-Splines, which can be subdivided into non-periodic and periodic

2. Non-uniform B-Splines

In non-periodic uniform B-Splines, the knots are uniformly spaced except at the ends where the knot values are repeated $p + 1$ times so that

$$U = \{\underbrace{0, 0, \ldots, 0}_{p+1}, u_{p+1}, \ldots, u_{m-p-1}, \underbrace{\alpha, \alpha, \ldots, \alpha}_{p+1}\} \tag{5}$$

The above knots are also referred to as non-periodic or open knots. Non-periodic B-Splines are infinitely continuously differentiable in the interior of a knot span, and $(p - k)$-times continuously differentiable at a knot. If $k = p$, we say that the knot has full multiplicity; the multiplicity cannot be greater than the degree. Multiplicity of knots provides a way to specify the continuity between segments. For example, a full multiplicity knot in the knot vector (away from the ends) means

7

that a kink or cusp is present in the curve. On the other hand, in periodic B-Splines, the knots are uniformly spaced but the first and last knots are not duplicated so that the knot vector looks like

$$U = \{0, 1, \ldots, n\} \tag{6}$$

Periodic B-Splines are everywhere $(p-1)$-times continuously differentiable.

If the knots are unequally spaced, the knot vector is non-uniform, we get non-uniform B-Splines (the NU part in NURBS). The non-uniformity in knots can cause the degree p of the curve to be different between knot spans. As a matter of terminology and in describing grain geometries, knot vectors can be defined in either $[0,1]$ or $[0,n]$. The choice of normalization does not have any effect on the shape of the curve, and it is therefore inconsequential.

Remark 2. Equation (3) is usually taken as the definition of NURBS although the non-uniformity of the knots is not obvious from this expression.

Remark 3. It is rare that one would work with NURBS models directly in parametric space. In practice, grain shapes are typically generated interactively or through some optimization procedure such as least squares.

2.1.4 Closing a NURBS curve

To reproduce grain geometries accurately, it is necessary to close the NURBS curves used to describe the grain surface. There are at least two procedures to close a NURBS curve. In the first procedure, closed NURBS curves are defined by 'wrapping' control points. In this process, a uniform knot sequence of $m+1$ knots is constructed such that: $u_0 = 0, u_1 = 1/m, u_2 = 2/m, \ldots, u_m = 1$. Note that the domain of the curve is $[u_p, u_{n-p}]$. Then, the first and last p control points are wrapped so that $\boldsymbol{P}_0 = \boldsymbol{P}_{n-p+1} = \boldsymbol{P}_{n-p+2}, \ldots, \boldsymbol{P}_{p-2} = \boldsymbol{P}_{n-1}$ and $\boldsymbol{P}_{p-1} = \boldsymbol{P}_n$. By grapping the control points, C^{p-1} continuity is ensured at the joining point $\boldsymbol{C}(u_p) = \boldsymbol{C}(u_{n-p})$.

In the second approach, the first and last control points are made coincident, i.e., $\boldsymbol{P}_0 = \boldsymbol{P}_n$ and the first and last $p+1$ knots are clamped, i.e., repeated. The curve may or may not have C^k continuity depending on how the first and last k internal knot spans are chosen, and the first and last $k+1$ weights and control points are chosen. Perhaps the simplest example is that of a unit circle in which the control points and weights shown in Table 1 are used together with the following

knot vertor

$$U = \{0, 0, 0, 1, 1, 2, 2, 3, 3, 4, 4, 4\} \tag{7}$$

We notice that $P_0 = P_8$ and the first and last three knot values are clamped. Also, there are three pairs of internal knots with multiplicity two. In general, this would lead to a loss of continuity in the first derivative. However, in this case, continuity in the first derivative is maintained by three collinear control points in each of the following sets: $\{P_7, P_0 = P_8, P_1\}$, $\{P_1, P_2, P_3\}$, $\{P_3, P_4, P_5\}$, and $\{P_5, P_6, P_7\}$.

i	x_i	y_i	w_i
0	1	0	1
1	1	1	$\sqrt{2}/2$
2	0	1	1
3	-1	1	$\sqrt{2}/2$
4	-1	0	1
5	-1	-1	$\sqrt{2}/2$
6	0	-1	1
7	1	-1	$\sqrt{2}/2$
8	1	0	1

Table 1: Control points (x_i, y_i) and weights w_i for a unit circle.

2.1.5 Relevance of NURBS to DEM calculations

To conclude this section, some of the advantages of using NURBS in the context of discrete element method calculations are listed. Some of the most salient mathematical properties of NURBS that make them ideal candidates for DEM calculations are [17; 18]:

1. Local support property

2. Invariance under affine transformations

3. Local curvature equation

4. Strong convex hull property

5. Integration with isogeometric finite elements

The local support property affords the method tremendous flexibility in the description of grain geometries. Local support implies that the basis function $N_{i,p}(u)$ is non-zero on $[u_i, u_{i+p+1})$. Since

the basis function $N_{i,p}(u)$ is the coefficient of control point $\boldsymbol{P}_i$, the product $N_{i,p}(u)\boldsymbol{P}_i$ changes if $\boldsymbol{P}_i$ changes, but the change in $N_{i,p}(u)\boldsymbol{P}_i$ only affects the segment on $[u_i, u_{i+p+1})$, leaving the rest of the curve $\boldsymbol{C}(u)$ unchanged. Therefore, because of local support, a change in the position of a control point, only affects the local portion of the NURBS curve, this allows great flexibility when trying to approximate grain boundaries accurately. Also, by the local support property, any modifications to the weights w_i, too, will only affect the section of the NURBS curve on the $[u_i, u_{i+p+1})$ interval.

On the other hand, the invariance property of NURBS under affine transformations is useful when updating the grains described using NURBS within the time integration scheme. Exploiting this property, the grains position is updated by simply translating and/or rotating the control points relative to the grains centroids.

NURBS provides a simple procedure for evaluating local curvatures. It is well known that contact stresses (e.g., Hertzian contact) depend on the radii of curvature of two contacting bodies. Evaluation of curvature for simple shapes such as circles and ellipses is straightforward but becomes complicated for arbitrary-shaped grains. In addition to providing the tangent and normal boundary vectors needed for contact force calculations, NURBS also provide local curvature evaluations that can be used directly in calculating local contact forces. After obtaining the first and second local derivatives $\boldsymbol{C}^{(1)}$ and $\boldsymbol{C}^{(2)}$, respectively, the curvature vector can be evaluated such that

$$\boldsymbol{\kappa} = \frac{\left(\boldsymbol{C}^{(1)} \cdot \boldsymbol{C}^{(1)}\right)\boldsymbol{C}^{(2)} - \left(\boldsymbol{C}^{(1)} \cdot \boldsymbol{C}^{(2)}\right)\boldsymbol{C}^{(1)}}{\left(\boldsymbol{C}^{(1)} \cdot \boldsymbol{C}^{(1)}\right)^2} \tag{8}$$

and consequently, the local radius of curvature is calculated such that $R = 1/\|\boldsymbol{\kappa}\|$.

The strong convex hull property ensures that, for a closed NURBS curve, the entire grain is located within the convex hull defined by the corresponding control points. Using the control points to define a convex hull bounding each grain, the granular entities described using NURBS can be easily incorporated into existing DEM global collision detection algorithms. We note that the control polygon defined by the control points could be non-convex. Also, the convex hull property fails for negative weights in which a portion of the affected curve segment will be outside of the convex hull defined by the corresponding control points. However, negative weights are not typically used when describing grain shapes and, therefore, convex hull failure is typically not a

concern.

Finally, the use of NURBS within the granular element method, provides a foundation for high-fidelity physics at the granular level. Since NURBS have recently been shown to furnish a basis for isogeometric finite element analysis [17], within each particle more complex analysis such as plasticity, damage, or breakage, can be performed exploiting the available basis functions for a given grain. Evidently, NURBS, within the context of GEM, can offer tremendous flexibility in representing and optimizing grain morphology, as well as provide important geometric properties that would enable higher-fidelity mechanics calculations for DEM.

Remark 4. As noted before, particle morphology is currently characterized at three length scales: sphericity, roundness, and roughness, respectively. Sphericity is defined at the scale of particle diameter and roundness is defined one scale below. Current tomography data is able to resolve morphology at these two levels and hence GEM can exploit this to represent the first two levels of morphology directly. However, particle roughness in GEM will rely on the concept of effective interparticle coefficient to account for this lower level of particle morphology. The advantage over current interparticle friction coefficients being used in DEM today is that the friction coefficient used to model roughness should be closer to reality and, therefore, more robust.

2.2 Discrete equations of motion

Since GEM is a variant of the original discrete element method (DEM), with the additional ability to represent particle morphology accurately, here we present the original equations of motion as in [4] for the sake of simplicity. Even though the equations of motion are standard and their integration is well documented, we present these developments here for completeness of presentation. Also, for simplicity, we limit our discussion to two dimensions, once again, noting the ability to go to three dimensions.

Our point of departure is furnished by the classical equations of equilibrium for a rigid particle, with damping, so that

$$
\begin{aligned}
ma_i + Cv_i &= F_i \\
I\alpha + \bar{C}\omega &= M
\end{aligned}
\tag{9}
$$

where $i = 1, 2$ in two dimensions, m and I are the mass and moment of inertia for the particle, respectively, $C = \xi m$ and $\bar{C} = \xi I$ are the coefficients of global damping acting on the linear velocity v_i and the angular velocity ω, respectively, with ξ being the global damping parameter. The linear acceleration is given by a_i and the angular acceleration is represented by α, and these are related to the resultant force F_i and moment M, respectively. As in classical DEM, the resultant force F_i and moment M acting on the particle are induced by contact interactions between particles. In this section, for purposes of integrating the equations of motion, we assume F_i and M are given.

In the time integration scheme, velocities are evaluated using the mid-point rule so that

$$
\begin{aligned}
v_i^n &= \frac{1}{2}\left(v_i^{n+1/2} + v_i^{n-1/2}\right) \\
\omega^n &= \frac{1}{2}\left(\omega^{n+1/2} + \omega^{n-1/2}\right)
\end{aligned}
\tag{10}
$$

where the superscripts refer to particular time-stations. Similarly, accelerations are approximated so that

$$
\begin{aligned}
a_i^n &= \frac{1}{\Delta t}\left(v_i^{n+1/2} - v_i^{n-1/2}\right) \\
\alpha^n &= \frac{1}{\Delta t}\left(\omega^{n+1/2} - \omega^{n-1/2}\right)
\end{aligned}
\tag{11}
$$

where we have used simple finite differences over a time increment Δt. Using the approximations obtained for the kinematics and using them in the equations of motion, we get an approximation for the velocities at $t_{n+1/2}$ such that

$$
\begin{aligned}
v_i^{n+1/2} &= \frac{1}{1 + \xi\Delta t/2}\left[(1 - \xi\Delta t/2)\, v_i^{n-1/2} + \frac{\Delta t}{m}F_i\right] \\
\omega^{n+1/2} &= \frac{1}{1 + \xi\Delta t/2}\left[(1 - \xi\Delta t/2)\, \omega^{n-1/2} + \frac{\Delta t}{I}M\right]
\end{aligned}
\tag{12}
$$

The linear and angular velocities are then used to update the corresponding displacements x_i and rotation θ of the particle

$$
\begin{aligned}
x_i^{n+1} &= x_i^n + \Delta t v_i^{n+1/2} \\
\theta^{n+1} &= \theta^n + \Delta t \omega^{n+1/2}
\end{aligned}
\tag{13}
$$

Exploiting the invariance of NURBS to affine transformations [18], the control points are updated at each time step through translation and rotation about the grain centroid, as specified above.

Finally, in DEM, damping is used to achieve quasi-static conditions by utilizing the so-called dynamic relaxation, which allows the dissipation of accelerations and hence making all resulting forces vanish, achieving in this way static equilibrium [23]. This procedure of dynamic relaxation is used in this paper in the context of GEM.

2.3 Contact force calculations

In this section, we illustrate how contact forces between two grains are calculated in the context of GEM. For simplicity, the adopted procedure is a generalization of that utilized in the contact calculation for circular grains and described in [4]. As shown in Figure 2, the procedure looks at two grains in contact, Ω_p and Ω_q, at a particular instant in time. Particle position is given by the centroid, with Ω_p and Ω_q having centroids located at $\boldsymbol{x}_c^p$ and $\boldsymbol{x}_c^q$, respectively. A local coordinate system (in 2D for simplicity) is adopted, where the normal direction (at the point of contact) is given by the unit vector $\boldsymbol{e}$, pointing away from particle Ω_p and the tangential direction furnished by the unit vector $\boldsymbol{t}$, which would induce a clockwise rotation of vector $\boldsymbol{e}$. Further, changes in angular position θ are assumed positive if they induce a counter-clockwise rotation of the particle, relative to the particle's centroid. Similarly, positive moments are assumed to induce positive rotations.

As illustrated in Figure 2, contact between two grains is detected when there is overlap between two grains. At this point, the following steps are performed in order to quantify the magnitude of contact:

1. Determine the two intersection points $\boldsymbol{x}^1$ and $\boldsymbol{x}^2$, and use these to establish the midpoint $\boldsymbol{x}^m = 1/2(\boldsymbol{x}^1 + \boldsymbol{x}^2)$.

2. Using points $\boldsymbol{x}^1$, $\boldsymbol{x}^2$, and $\boldsymbol{x}^m$, construct and place normal and tangential unit vectors $\boldsymbol{e}$ and $\boldsymbol{t}$, respectively. The tangential vector is defined such that $\boldsymbol{t} = (\boldsymbol{x}^2 - \boldsymbol{x}^1)/\|\boldsymbol{x}^2 - \boldsymbol{x}^1\|$ and $\boldsymbol{e} \cdot \boldsymbol{t} = 0$ is used to obtain $\boldsymbol{e}$. Both unit vectors define a basis centered at $\boldsymbol{x}^m$.

3. Determine the two intersection points $\boldsymbol{x}^3$ and $\boldsymbol{x}^4$. These points are obtained by the intersection of a straight line in the direction of $\boldsymbol{e}$ with the boundaries of grains Ω_p and Ω_q, respectively.
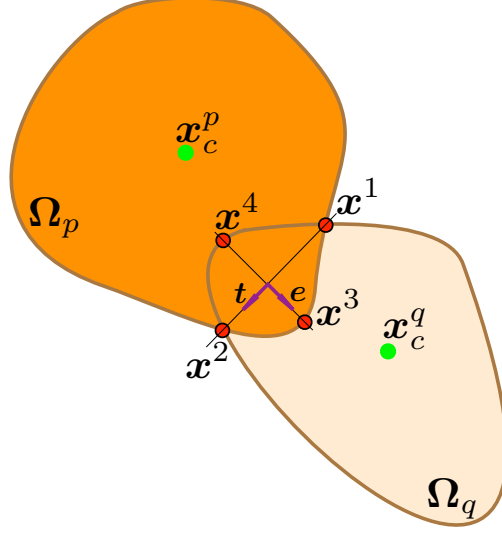
Figure 2: Illustration of two particles (Ω_p and Ω_q) in contact showing interpenetration (overlapping). Particles have centroids described by x_c^p and x_c^q corresponding to Ω_p and Ω_q, respectively. Note, overlapping area is exaggerated for illustrative purposes.

4. Approximate the overlap distance between grains Ω_p and Ω_q such that $\Delta n = \|x^4 - x^3\|$.

5. Compute the moment arms $\boldsymbol{R}^p = x^3 - x_c^p$ and $\boldsymbol{R}^q = x^4 - x_c^q$.

We note that the definition of the contact plane for an arbitrary shaped grain is not unique. The way the contact plane is defined in step 1 above is referred to as the usual approach, which is passing the plane through the intersection points [11]. There are also other approaches to defining the overlap such as passing the contact forces through the centroid of the overlapping area. Another approach is the common plane method described in [24]. For smooth boundaries, the approach defined above is a reasonable approximation. Then, we use the above calculations to compute the forces exerted on the grains and the associated moments. We split the calculations into normal and tangential components for clarity.

2.4   Normal force and associated moments

The effective normal contact force is calculated using a linear elastic stiffness model such that

$$F_n = k_n \left(\Delta n + \beta \dot{n} \right) \tag{14}$$

14

where k_n is the normal elastic stiffness, β is the contact damping parameter and $\dot{n}$ is the normal component of the relative velocity of grain Ω_p relative to grain Ω_q so that

$$\dot{n} = (\dot{\boldsymbol{x}}_c^q - \dot{\boldsymbol{x}}_c^p) \cdot \boldsymbol{e} \tag{15}$$

The normal force F_n is exerted on grain Ω_p in the $-\boldsymbol{e}$ direction and on Ω_q it is exerted in the $\boldsymbol{e}$ direction, exploiting action and reaction. Similarly, the moments due to the excentricity of the normal contact force is exerted on the centroid of particles Ω_p and Ω_q, respectively, such that

$$M_n^p = -F_n R_s^p \qquad \text{and} \qquad M_n^q = F_n R_s^q \tag{16}$$

where $R_s^p = \boldsymbol{R}^p \cdot \boldsymbol{t}$ is the tangential component of the $\boldsymbol{R}^p$ moment arm, and $R_s^q = \boldsymbol{R}^q \cdot \boldsymbol{t}$ is the tangential component of the $\boldsymbol{R}^q$ moment arm. Note that we have exploited action and reaction. Also, when the particle shapes are circular, the above moments are nil and the calculations reduce to those of the classic DEM [4].

2.5 Tangential force and associated moments

For the sake of simplicity, the incremental tangential forces are calculated here using the friction model proposed in [4]. In this model, the tangential stiffness is initialized at time of first contact and exists until the grains separate. The increment in shear force is calculated such that

$$\Delta F_s = k_s \left(\Delta s + \beta \dot{s} \right) \tag{17}$$

where $\dot{s}$ is the relative tangential velocity of grain Ω_p with respect to grain Ω_q, and it is calculated so that

$$\dot{s} = (\dot{\boldsymbol{x}}_c^p - \dot{\boldsymbol{x}}_c^q) \cdot \boldsymbol{t} - (\omega^p R_s^p + \omega^q R_s^q) \tag{18}$$

where ω^p and ω^q are the angular velocities of grains Ω_p and Ω_q, respectively. Naturally, $\Delta s = \dot{s} \Delta t$ and the relative velocity $\dot{s}$ is taken as possitive when pointing in the $\boldsymbol{t}$ direction and negative if it points in the $-\boldsymbol{t}$ direction. At a discrete time station t_{n+1} the shear force is then updated according

to

$$F_s = F_s^n + \Delta F_s \tag{19}$$

where F_s^n is the value of the tangential force at time station t_n. Ultimately, the tangential force is limited according to Coulomb-friction law so that

$$F_s = \min(F_s, \mu F_n + c) \tag{20}$$

where μ is the interparticle friction coefficient of friction and c is the interparticle cohesion. The tangential force is applied on grains Ω_p and Ω_q in the directions $-\boldsymbol{t}$ and $\boldsymbol{t}$, respectively, for $\dot{s} > 0$, and in the opposite directions otherwise.

Similar to the normal component of the contact force, the shear component of the force exerts moments with respect to the centroids of the grains in contact. The resulting moments are calculated such that

$$M_s^p = F_s R_n^p \qquad \text{and} \qquad M_s^q = -F_s R_n^q \tag{21}$$

with $R_n^p = \boldsymbol{R}^p \cdot \boldsymbol{e}$ is the normal component of the $\boldsymbol{R}^p$ moment arm and $R_n^q = \boldsymbol{R}^q \cdot \boldsymbol{e}$ is the normal component of the $\boldsymbol{R}^q$ moment arm.

Remark 5. Our choice of contact model is solely guided by simplicity. Linear contact using interpenetration calculations, as illustrated in the above procedure, are as simple as it gets. This approach is a generalization of current intersection-based algorithms similar to those used for ellipses [13; 25; 26] and polyhedra [11]. It is clear that GEM will be able to incorporate more complex contact models such as Hertz-Mindlin, where geometric aspects such as curvature play a crucial role. Other geometric information such as tangential and normal directions at contact is also available and could be exploited for modeling purposes. The effects of the choice of contact model remain unknown but GEM offers a platform for studying these effects systematically.

3 Estimated computational cost of GEM

In this section, we present a preliminary (somewhat conservative and mostly applicable to 2D conditions) estimate on the computational expense associated with the granular element method

(GEM) proposed in this paper. Given that most components of GEM are identical to standard DEM, the two natural and central questions concerning the cost of GEM are: 1. how many control points or spline segments do we need in order to have accurate grain morphology representation and 2. what is the cost of performing curve-curve intersection checks. Here, we put the cost of GEM in perspective by making rough comparisons with other established DEM techniques such as clumping and polyhedra.

3.1 Number of control points and spline segments

In the granular element method (GEM) a significant part of the computational expense involved is devoted to curve-curve intersection checks for local (the so-called narrow phase) contact resolution. The initial step in local contact resolution is to search through the spline curve for potential contacting segments. In NURBS, the number of spline segments is related to the number of control points. For example, if we define a closed curve by wrapping control points in a NURBS curve as described in Section 2.1.4, then the number of spline segments, excluding the wraparound segments, is given by $n + 1 - p$ where $n + 1$ is the total number of control points and p is the degree of the curve. Note that, to reduce computational expenses, the search algorithm uses the control polygon, not the actual spline curve.

Figure 3 shows a two dimensional representation of a sand grain image using the overlapping rigid cluster method (ORC) [6] and NURBS. Both methods target 99% area coverage and NURBS naturally matches local curvature as well. It can be seen that thirteen (13) discs are needed to capture the particle shape using ORC whereas NURBS needs 34 control points, including three overlapping control points. In 2D, NURBS will need between 20 to 40 spline segments to represent grain morphology accurately, while it has been estimated that the ORC method will need about 10-20 discs [27]. Polyhedra-based DEM would need a similar number of segments as NURBS. It should be noted that NURBS naturally captures local curvature of the particle, something that proves quite challenging for both clumping and polyhedra methods. For instance, it can be seen in Figure 3 that the ORC method cannot capture local curvature of the particle since at a given portion of the particle boundary, the curvature is approximated by a circle. Similarly, in the polyhedra method, a segment of the particle is approximated by a straight line in 2D. Local curvature information is important in calculating nonlinear contact forces such as those furnished by Hertzian contact laws.
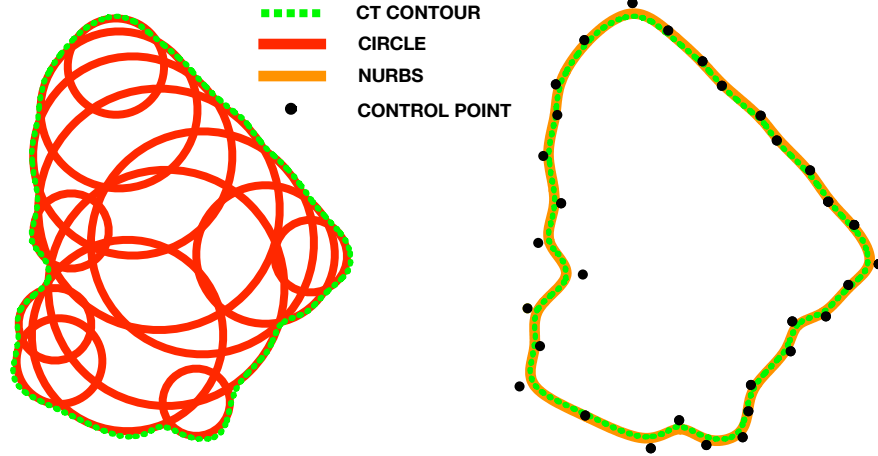
Figure 3: Two-dimensional representation (projection) of a sand grain image using the ORC method (left) and NURBS (right). Both methods target 99% area coverage. Particle image using ORC taken from [27].

Since the ORC method only requires information about the centroid and radius of the particles, it is expected that this method will be cheaper than GEM in terms of contact calculations. However, as noted above, ORC will only provide an approximation of local curvature. As for the polygon-based methods, they will need similar number of segments as GEM, but contact detections and resolution will be cheaper given the simpler linear geometry. As in ORC, polygon methods will incorrectly represent local curvature. GEM will capture shape and local curvature at the expense of intersection checks.

3.2 Intersection checks

The main difference between GEM and clumping (e.g., ORC) and polyhedra methods, is that NURBS are in general nonlinear representations, and therefore will require iterations to determine the location of intersection points. On the other hand, polyhedra methods furnish analytical procedures for contact point detection owing to their linear nature. Clumping methods such as ORC detect contact directly since the overlapping distance is determined when the distance between two circles centroids is less than the sum of their radii.

To further appreciate the computational cost associated with the intersection checks required by GEM, it is necessary to discuss how the intersection algorithm works. The basic spline intersection

18

problem is to solve the following vector equation [28]

$$\boldsymbol{C}(s) = \boldsymbol{C}(t) \tag{22}$$

where $\boldsymbol{C}(s)$ and $\boldsymbol{C}(t)$ are two spline curves parametrized by s and t, respectively. Several methods are available to solve this problem in practice.

The spline intersection algorithm utilized in GEM is based on recursive subdivision and a Newton-Raphson iterative scheme [29; 30]. Using this approach, uniform subdivision of the control polygons is first performed until the control polygons come sufficiently close to the spline curves. Then, the intersection points between the polygons are used as approximations to start a Newton-Raphson iteration to solve the nonlinear problem given in equation (22). Naturally, the uniform subdivision is of linear order, but provided that the grain geometry is accurately represented, the corresponding control polygon would already be lying quite close to the spline curve (cf., Figure 3), so the number of subdivisions is small.

There are other spline intersection algorithms that do not use Newton-Raphson's method but are iterative nonetheless. For example, Bézier clipping [31] is a variation on the subdivision approach that clips away the regions of the curves where no intersections can take place and this has been shown in [32] to lead to a quadratically convergent method. Another algorithm is presented in [28], which requires no starting point and is asymptotically Newton-like.

Based on the area coverage requirement alone, GEM is slightly more expensive than polyhedra-based DEM because of the additional expense required to iterate to find the intersection points. The cost of GEM and polyhedra-based DEM may become comparable if high accuracy in curvature is required, in which case the number of segments in polyhedra-based DEM is increased at sections of high curvature. The research on spline intersection algorithms is very active and there is also interesting developments in GPU-accelerated intersection algorithms (e.g., [33]). In the future, some of these algorithms could be assimilated into GEM to offset the expense of iterating.

Remark 6. In the above section, we have sketched the main sources of computational cost for GEM and have attempted to contrast these with existing methods. However, a proper benchmark is still missing and will have to be conducted in the near future to be truly able to assess the cost of GEM compared with other methods that also try to capture particle morphology such as ellipsoids,

polyhedra, clumping, etc. In this portion of the work, we have focused on introducing the method and its main features, rather than assessing its computational cost directly.

4   Numerical examples

In this section, we present two numerical examples to showcase the granular element method (GEM) capabilities. Both examples are two-dimensional and quasi-static in which sufficient numerical damping is applied to achieve static equilibrium. The first example, is the classic nine-disc test performed in [4] and serves here as a verification exercise. The second example is richer and it entails a granular assembly of fifteen angular grains sheared in plane strain conditions. This latter example shows GEM's ability to do calculations with arbitrarily complex shapes.

4.1   Nine-disc test

This example serves as a verification of GEM's ability to represent circular sections using NURBS, as well as its ability to reproduce previously obtained results in this field. Hence, this example is identical to the nine-disc test reported in [4]. An assembly of nine (9) discs is packed in simple cubic configuration within rigid walls, as shown in Figure 4. All nine discs are identical, with radius of 50 units and density of 1000 units. Two different contact stiffnesses are used in these calculations: $k_n = 1.35e9$ and $k_n = 1.5e8$, with shear contact stiffness taken as $k_s = k_n$, unless otherwise noted. Also, the interparticle friction coefficient $\mu = \tan \phi$ where ϕ is the internal friction angle. In this test, $\phi = 15°$, unless otherwise noted. The nine-disc test is subdivided into two loading scenarios: uniform compression and pure distortion.
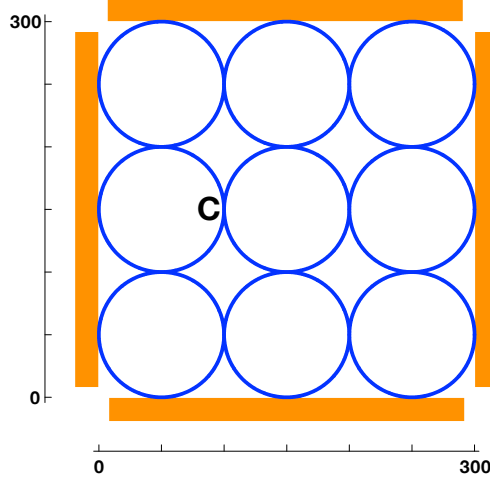
Figure 4: Initial configuration for nine-disc test.

4.1.1 Uniform compression test

In this test, all four walls are moved inwards with speed v_{wall} for a total duration T_{wall}. Wall motion is then stopped at that point T_{wall} and the test is allowed to continue until a total of 200 cycles is reached. The loading sequences in this test are summarized in Table 2.

Table 2: Loading cases for uniform compression test

Case	No.	Disc Stiffness $k_n = k_s$	Δt	T_{wall} (cycles)	v_{wall}
(a)	1	1.35e9	0.01525	40	0.12
	2			120	0.04
(b)	1	1.5e8	0.04576	40	0.36
	2			120	0.12

In this test, the effect of global numerical damping ξ, as it appears on the global equations of motion, is investigated (cf., equation (9)). Figure 5 shows the evolution of normal force at point C for case (a) number 1 (see Table 2). Normal force evolution is reported for the case when there is global numerical damping ($\xi = 3$) and for the case when there is no global damping ($\xi = 0$). No contact damping β is used on any of the results reported herein. The results shown in Figure 5 exactly match those reported in [4] and clearly show the effect of damping in reducing the amplitude of oscillations, allowing kinematics and corresponding forces to reach steady-state equilibrium. Finally, the evolution of the normal force F_n at point C is shown in Figure 6. It can be seen from this figure that all loading cases converge to roughly the same value of force after a

21

number of cycles when steady equilibrium is achieved.
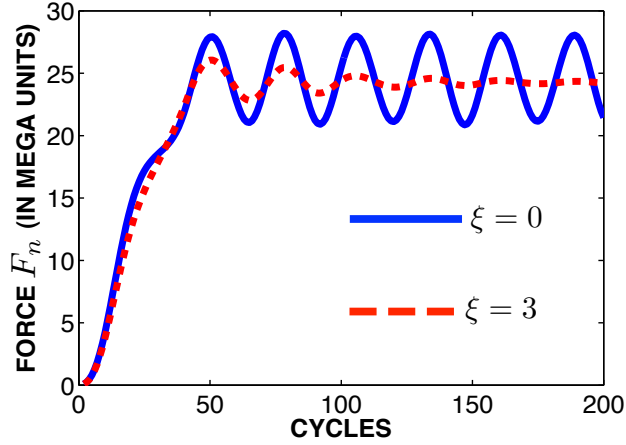

Figure 5: Normal force F_n evolution at C for loading case (a) No. 1 at different values of global numerical damping.
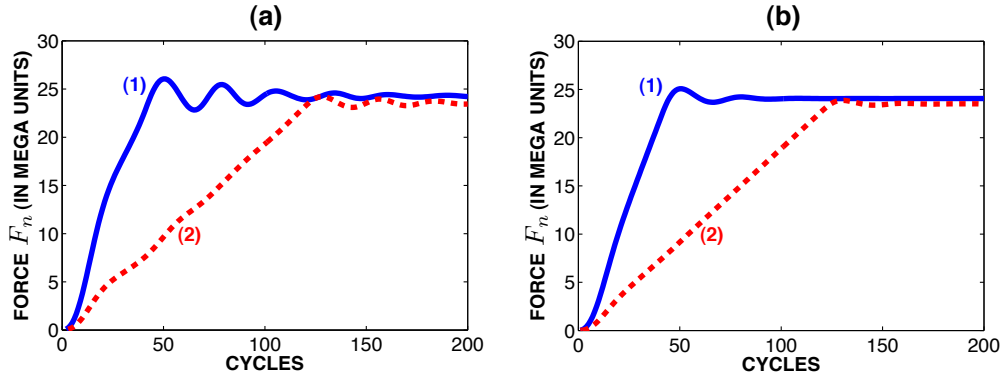

Figure 6: Evolution of normal force F_n for all loading cases reported in Table 2 with global numerical damping $\xi = 3$.

4.1.2 Distortion test

Here, we reproduce the distortion test for the nine-disc configuration reported in [4]. This constitutes the second half of the verification process and it is performed following the loading sequence reported in [34], which thoroughly describes the distortion test shown in the original work of Cundall and Strack [4]. Similar characteristics as in Case (a) No. 1 shown in Table 2 are used here, with $k_n = 1.35e9$ and $\Delta t = 0.01525$. The sample is initially uniformly compressed, as in the

22

uniform compression test, for 4000 cycles with wall speed $v_{wall} = 0.12$, as before. Wall motion is then stopped, followed by 1000 cycles where oscillations are allowed to settle via global numerical damping $\xi = 3.0$. As before, no contact damping was used (i.e., $\beta = 0$). After this uniform and settlement stage (total of 5000 cycles), constant volume distortion is prescribed by rotating the side walls at a constant angular velocity of 0.0175 for 500 cycles. The deformed configuration of the assembly after the first 5000 cycles of uniform compression and settlement, and the subsequent 500 cycles of constant-volume distortion are shown in Figure 7.
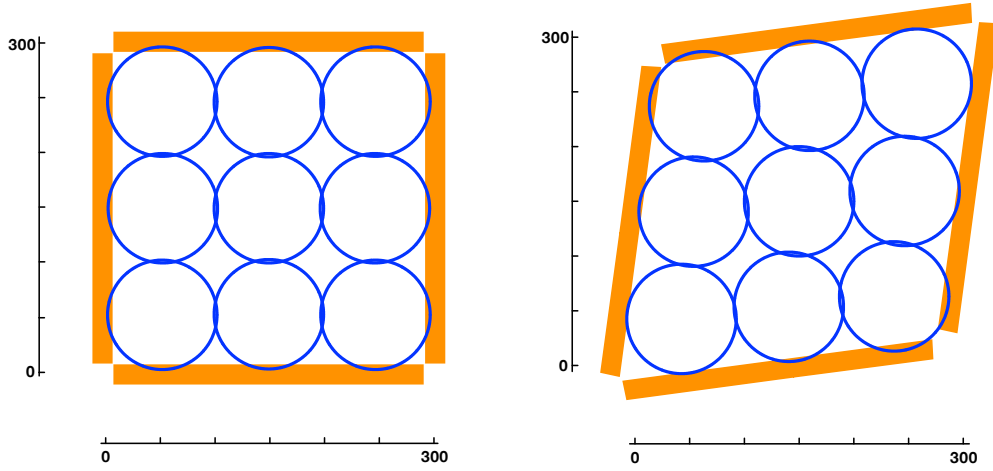
Figure 7: Distorted configurations for 9-disc assembly after 5000 cycles of uniform compression and settlement (left), and after subsequent 500 cycles of constant volume (shear) distortion (right). Results shown correspond to case when $k_n = k_s$ and interparticle friction angle $\phi = 30°$.

The evolution of the normal force F_n and shear force F_s at C is shown in Figure 8. Curves are shown for different values of interparticle friction coefficient $\mu = \tan \phi$ at various ratios of normal to shear contact stiffness k_s/k_n. The ratio k_s/k_n was shown by Mindlin [35] to vary from 2/3 to 1 for the case of linear elastic bodies in contact with elliptical contact areas. The extreme values of this range was investigated in [4] and is also reported here in Figure 8. The evolutions shown in Figure 8 agree quantitatively with the results obtained in [4; 34] and show the importance of interparticle friction (particle roughness) and the role of contact stiffness as modeled by the ratio k_s/k_n.
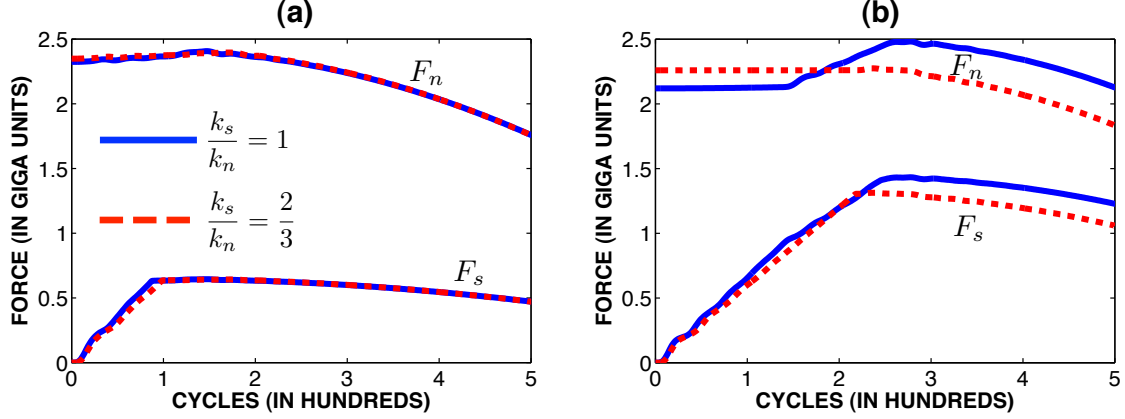
Figure 8: Normal and shear force evolution at point C in nine-disc assembly during 500 cycle shear distortion at various k_s/k_n ratios. (a) Interparticle friction angle $\phi = 15°$. (b) Interparticle friction angle $\phi = 30°$.

4.2 Fifteen-grain test

In this example, we use GEM to simulate a 15-grain assembly to showcase its ability to capture irregular shapes and to illustrate the importance of shape in the macroscopic response. As in the 9-disc test presented above, the sample is initially isotropically deformed and then subsequently sheared. Further, to highlight the importance of grain morphology, an equivalent circular assembly is constructed and distorted for comparison purposes. Micromechanical properties, such as force chains, are linked to macroscopic properties such as Mohr-Coulomb shear strength. This helps showcase the importance of micromechanical modeling in the development of macroscopic models via multiscale approaches [36]. Figure 9 shows the initial configuration for the 15-grain angular assembly using GEM and the equivalent assembly of 15 discs. All properties in both assemblies are identical, except for the shape of the particles, of course. The contact stiffness used is $k_n = k_s = 1.5e8$ and the time step is $\Delta t = 0.01$. Interparticle friction angle is $\phi = 15°$ and all grains have a density of 1000 units.

As in the nine-disc test, the deformation is strain-controlled, with all four walls acting as rigid boundaries with prescribed kinematics. The loading sequence is defined as follows. First, a uniform compression is performed by moving all four walls inwards with speed $v_{wall} = 0.2$. The uniform compression is performed in steps: compression is performed for the first 1000 cycles to close the initial grain separations, followed by 6 steps of 500-cycle hold and 500-cycle compression. After a
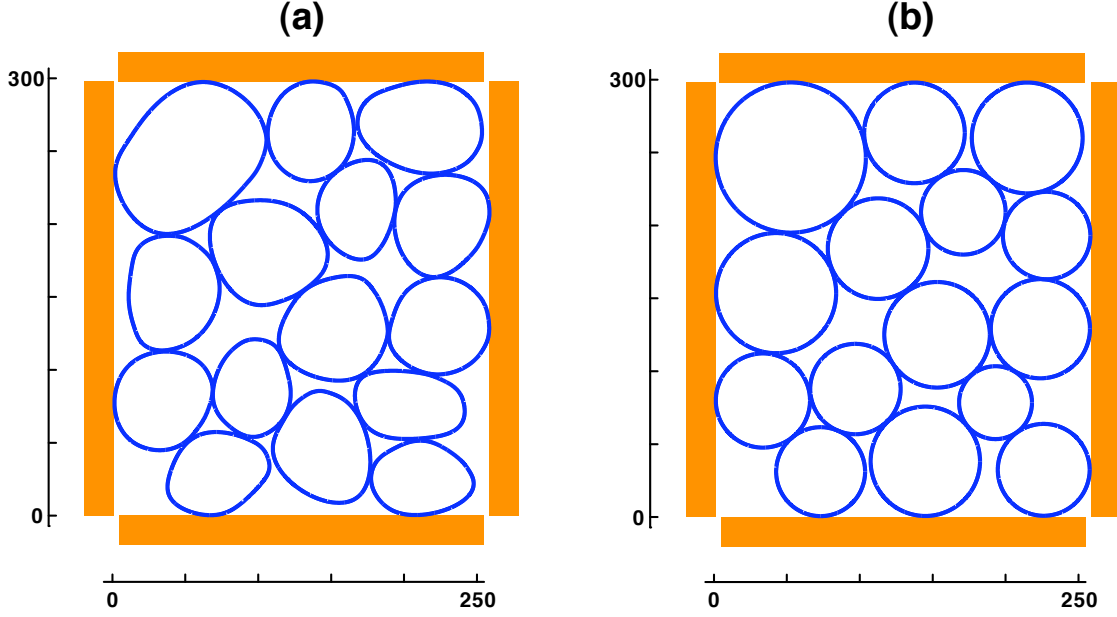
Figure 9: Initial configuration for fifteen-grain test: (a) GEM (b) Discs

total of 7000 cycles, wall motion is stopped and we wait for 1000 cycles. This is then followed by a constant volume distortion by rotating the walls at an angular velocity of 0.0175 for 500 cycles. For this test, we use a numerical damping parameter $\xi = 3.0$ and no contact damping.

To illustrate the role of particle morphology and its influence on macroscopic stresses, we calculate the interparticle contact forces and the corresponding macroscopic stresses in the assembly as a function of time. These developments showcase the direct link between micromechanical properties, such as interparticle forces, and macroscopic properties, such as stress. It has been shown before that, for a macroscopic domain Ω containing N_p number of particles, the average macroscopic stresses in a volumetric assembly of granular materials is defined as [5; 37].

$$\langle \boldsymbol{\sigma} \rangle := \frac{1}{\Omega} \int_\Omega \boldsymbol{\sigma} \mathrm{d}\Omega \equiv \frac{1}{\Omega} \sum_{p=1}^{N_p} \Omega_p \bar{\boldsymbol{\sigma}}^p \tag{23}$$

where

$$\bar{\boldsymbol{\sigma}}^p = \frac{1}{\Omega_p} \sum_{\alpha=1}^{N_c^p} \mathrm{sym}\left(\boldsymbol{f}^\alpha \otimes \boldsymbol{x}^\alpha\right) \tag{24}$$

is the average particle stress and N_c^p is the number of contact forces exerted on particle Ω_p. The vectors $\boldsymbol{f}^\alpha$ and $\boldsymbol{x}^\alpha$ represent the α-th contact force exerted on particle Ω_p and its location, respec-

25

tively. In this case, we have $N_p = 15$ and we calculate the average macroscopic stress implied in the granular assembly as induced by the distortional process imposed. This macroscopic stress $\langle \boldsymbol{\sigma} \rangle$ as a function of the microscopic state, namely $\boldsymbol{f}^\alpha$ and $\boldsymbol{x}^\alpha$, has been shown to be key in multiscale modeling and in the derivation of physics-based constitutive relations [36].

The numerical results obtained using these two assemblies are compared in Figures 10 through 12. We see that with even a small difference in grain morphology, the macroscopic average stresses and force chains patterns become significantly different because of the different contact topologies between the two assemblies. Figure 10 shows the evolution of the macroscopic stress tensor components. We observe that for both angular and disc assemblies, during the first 8000 cycles the macroscpic state of stress is isotropic with $\langle \sigma_{11} \rangle \approx \langle \sigma_{22} \rangle$ and $\langle \sigma_{12} \rangle \approx 0$. So, qualitatively, the macroscopic state of stress $\langle \boldsymbol{\sigma} \rangle$ for both the GEM (angular) and the disc assemblies shows the same trends. Quantitatively, however, the macroscopic pressure on the disc assembly is significantly larger due to differences in contact force topologies (see Figures 11 and 12). Same is true for the evolution of the macroscopic shear stress $\langle \sigma_{12} \rangle$ once the distortional phase is activated from cycle 8000 to 8500. There is a significant difference in the value of the macroscopic shear stress, with the disc assembly mobilizing larger shear stresses $\langle \sigma_{12} \rangle$ given the same macroscopic deformation.

Another interesting difference between the two assemblies is that, as shown in Figure 10, the macroscopic shear strength in the GEM assembly is significantly higher than that of the disc assembly. Specifically, Mohr-Coulomb strength criterion for the current state of stress requires $\sin \psi \approx |\langle \sigma_{12} \rangle / \langle \sigma_{11} \rangle|$ where ψ here is the macroscopic friction angle and a key measure of macroscopic strength in granular materials. At the end of the deformation process given by cycle 8500, the mobilized macroscopic friction angle for the GEM assembly is $\psi \approx 22°$, whereas $\psi \approx 14°$ for the disc assembly. This difference in mobilized strength can be attributed to the higher mean normal stress generated in the disc assembly for relatively similar shear stresses.

Figures 11 and 12 show snapshots of the corresponding interparticle forces and principal stresses at the particle level after volumetric compression (at cycle 8000) and shear distortion (cycle 8500). As in the previous plots, comparing the results for the angular (GEM) assembly and the disc assembly, one can observe qualitative similarities, but clear quantitative differences. The most striking quantitative difference is the relatively higher interparticle contact forces in the disc assembly after the compression stage, which leads to higher macroscopic mean normal stresses. This in turn leads
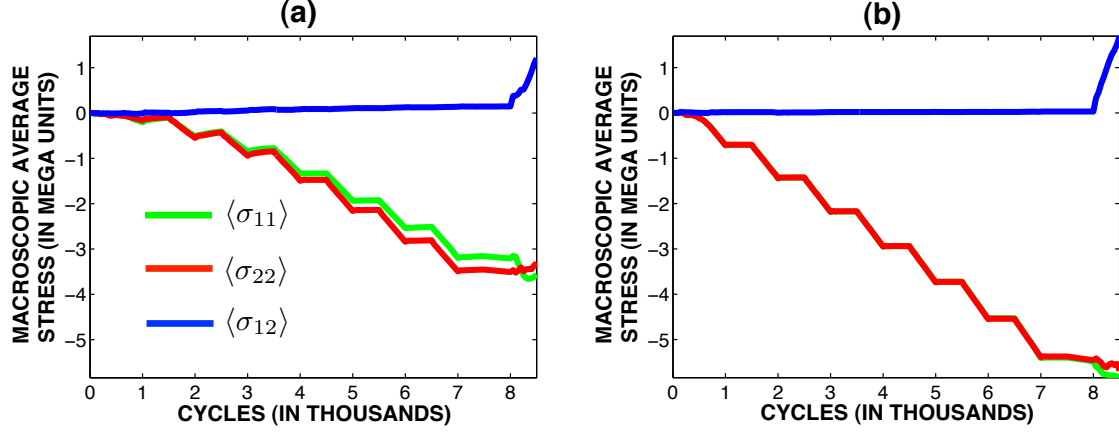
Figure 10: Evolution of components of the average macroscopic stress: (a) GEM (b) Discs

to lower macroscopic strength ψ, as shown above. It is interesting to note that after shear distortion, a clear force chain forms diagonally in both assemblies and that the principal stress directions at the granular level are on average aligned with the direction of principal stresses macroscopically.

The presented results showcase the ability of GEM to account for complicated load paths through a granular assembly because of the geometrical enhancement of the grain shapes provided by NURBS. Also, it is shown that accurate granular modeling will quantitatively affect macroscopic states, such as stress, and therefore, will make a significant difference in multiscale analysis and the development of accurate constitutive models.
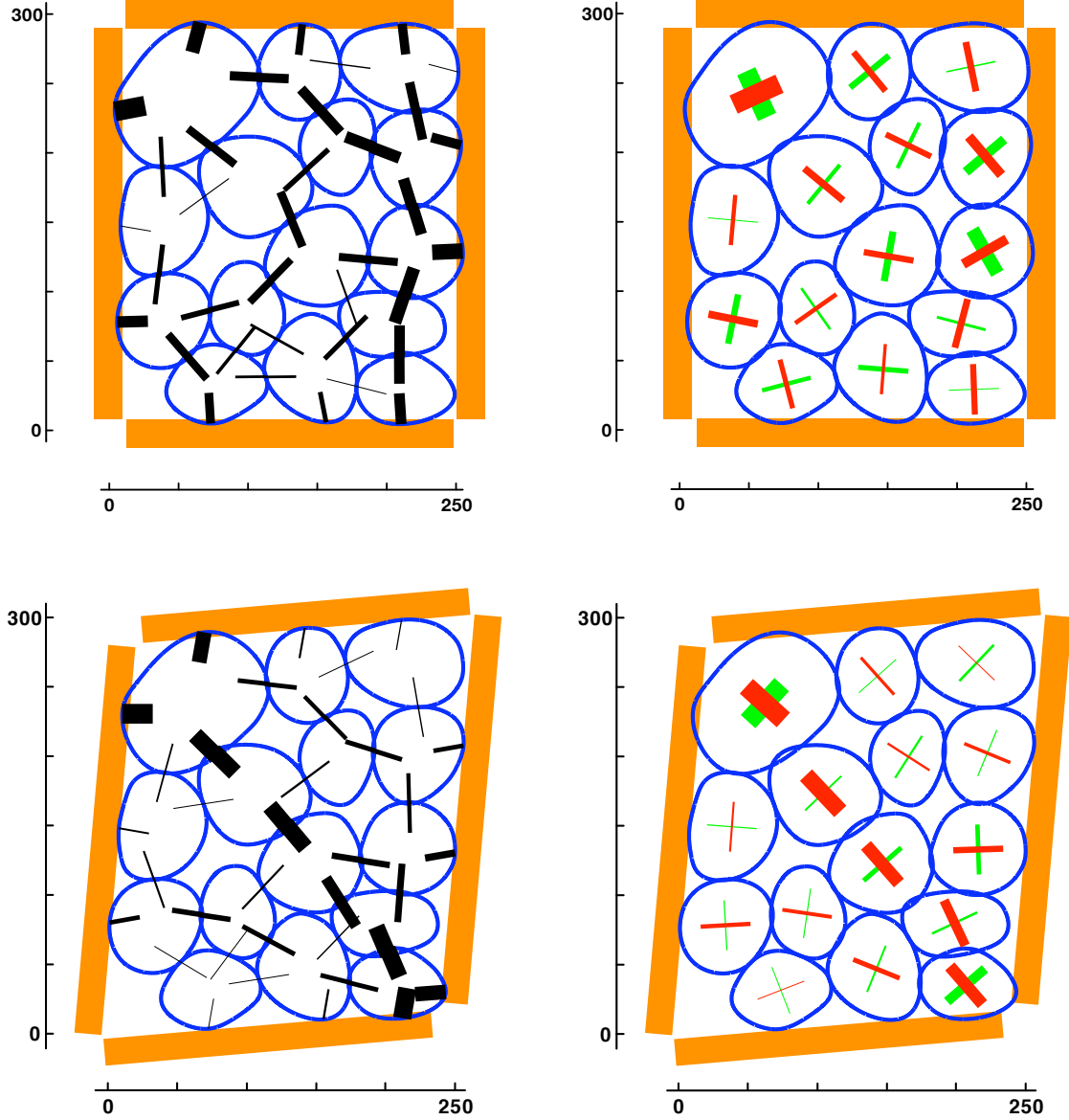
Figure 11: Distorted configurations for 15-GEM assembly at cycle 8000 (top) and cycle 8500 (bottom). Left figures show the interparticle contact forces (thickness proportional to force magnitude). Right figures show average principal stresses and directions in each particle (red lines are most compressive stresses; green lines are least compressive stresses).
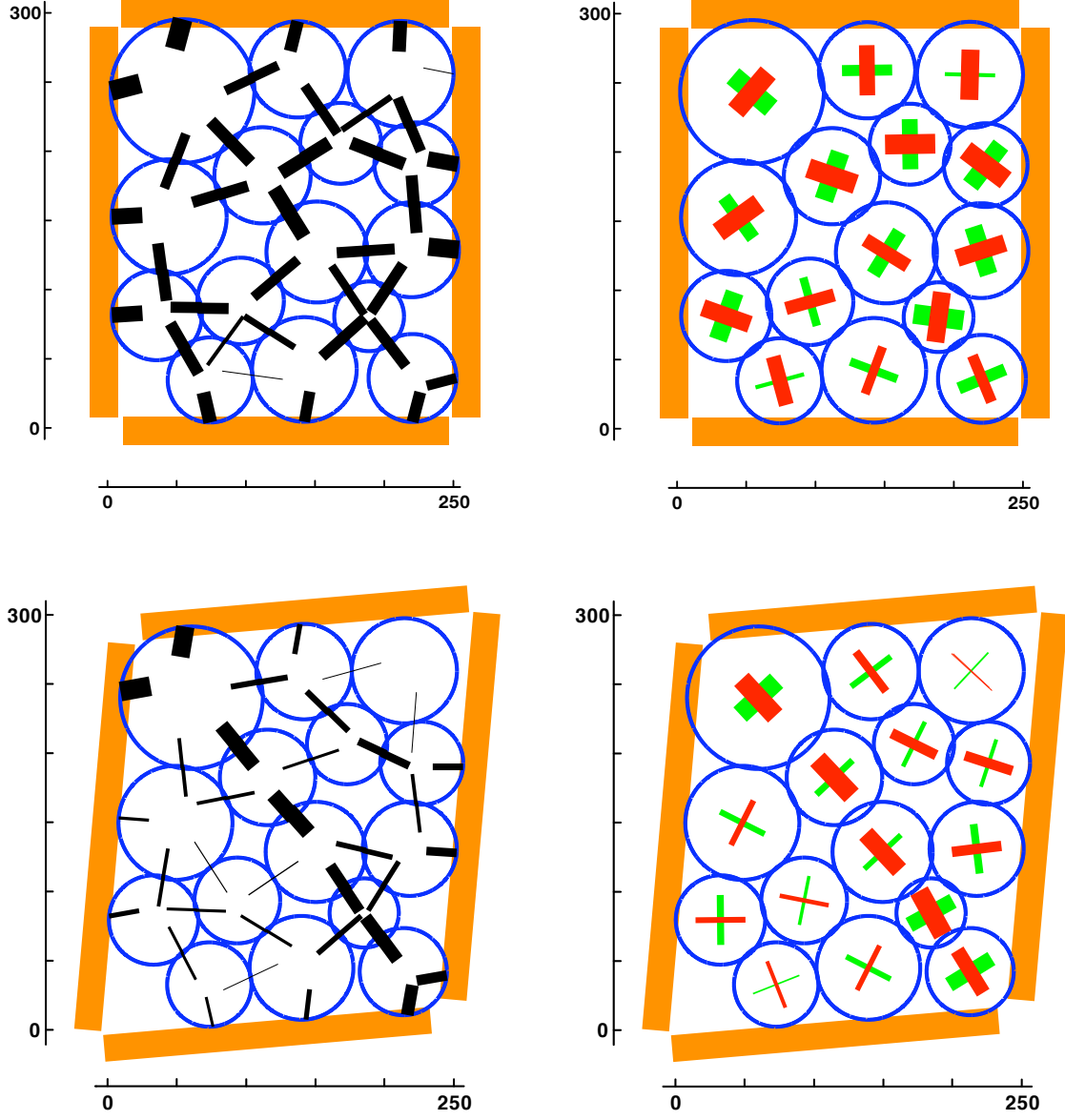
Figure 12: Distorted configurations for 15-disc assembly at cycle 8000 (top) and cycle 8500 (bottom). Left figures show the interpaticle contact forces (thickness proportional to force magnitude). Right figures show average principal stresses and directions in each particle (red lines are most compressive stresses; green lines are least compressive stresses).

5 Conclusion

We have presented a novel procedure called the Granular Element Method (GEM) for computational particle mechanics. This method provides geometrical enhancements of grain shapes through the flexibility of Non-Uniform Rational Basis-Splines (NURBS). Grain geometrical information can be directly obtained from advanced experiments using visualization tools such as X-ray CT, already available for natural granular materials such as sands. Also, we have shown that the implementation of GEM is straightforward, with all other standard DEM procedures remaining intact. The computational cost of GEM is slightly higher than polyhedra-based DEM due to the nonlinearity of NURBS and the need for iterations to find curve intersections. This cost, however, can be offset through more efficient intersection algorithms. Further work in the algorithmic aspects is required to make GEM competitive with conventional DEM. It is also expected that the additional costs be offset by the gains in accuracy. It is anticipated that GEM, coupled to experiments with X-ray CT, will be used in future experiments to infer interparticle contact forces in real assemblies under macroscopic loads, and to connect continuum representations and the discrete states via multiscale and homogenization techniques. These procedures could open the door to more physics-based constitutive models for science and engineering without having to rely on phenomenological approaches.

References

[1] G. C. Cho, J. Dodds, and J. C. Santamarina. Particle shape effects on packing density, stiffness, and strength: Natural and crushed sands. *Journal of Geotechnical and Geoenvironmental Engineering*, 132(5):591–602, 2006.

[2] B. Sukumaran and A. K. Ashmawy. Quantitative characterisation of the geometry of discrete particles. *Geotechnique*, 51:619–627, 2001.

[3] X. Garcia, L. T. Akanji, M. J. Blunt, and S. K. Matthai abd J. P. Latham. Numerical study of the effects of particle shape and polydispersity on permeability. *Physical Review E*, 80:021304, 2009.

[4] P. A. Cundall and O. D. L. Strack. A discrete numerical model for granular assemblies. *Géotechnique*, 29:47–65, 1979.

[5] J. Christoffersen, M. M. Mehrabadi, and S. Nemat-Nasser. A micromechanical description of granular material behavior. *Journal of Applied Mechanics*, 48:339–344, 1981.

[6] A.K. Ashmawy, B. Sukumaran, and A. V. Hoang. Evaluating the influence of particle shape on liquefaction behavior using discrete element method. In *Proceedings of the thirteenth international offshore and polar engineering conference (ISOPE 2003) Honolulu, Hawaii*, May 2003.

[7] X. Garcia and J.-P. Latham; J. Xiang; J.P. Harrison. A clustered overlapping sphere algorithm to represent real particles in discrete element modelling. *Geotechnique*, 59:779–784, 2009.

[8] P. A. Cundall. Formulation of a three-dimensional distinct element model - Part I: A scheme to detect and represent contacts in a system composed of many polyhedral blocks. *International Journal of Rock Mechanics and Mining Sciences*, 25(3):107–116, 1988.

[9] Y. M. A. Hashash D. Zhao, E. G. Nezami and J. Ghaboussi. Three-dimensional discrete element simulation for granular materials. *Engineering Computations*, 23:749–770, 2006.

[10] F. Alonso-Marroquin and H. J. Herrmann. Calculation of the incremental stress-strain relation of a polygonal packing. *Physical Review E*, 66:021301, 2002.

[11] A. A. Peña, P. G. Lind, and H. J. Herrmann. Modeling slow deformation of polygonal particles using dem. *Particuology*, 6:506 – 514, 2008.

[12] C. O'Sullivan. *Particulate Discrete Element Modelling: A Geomechanics Perspective*. Applied Geotechnics. Spon Press/Taylor & Francis, 2011.

[13] L. Rothenburg and R. J. Bathurst. Numerical simulation of idealized granular assemblies with plane elliptical particles. *Computers and Geotechnics*, 11(4):315 – 329, 1991.

[14] J. M. Ting, M. Khwaja, L. R. Meachum, and J. D. Rowell. An ellipse-based discrete element model for granular materials. *International Journal for Numerical and Analytical Methods in Geomechanics*, 17(9):603–623, 1993.

[15] G. T. Houlsby. Potential particles: a method for modelling non-circular particles in DEM. *Computers & Geotechnics*, 36:953–959, 2009.

[16] D. F. Rogers. *An Introduction to NURBS With Historical Perspective*. Academic Press, San Diego, 2001.

[17] T. J. R. Hughes, J. A. Cottrell, and Y. Bazilevs. Isogeometric analysis: CAD, finite elements, NURBS, exact geometry and mesh refinement. *Computer Methods in Applied Mechanics and Engineering*, 194:4135–4195, 2005.

[18] L. Piegl and W. Tiller. *The NURBS book (2nd ed.)*. Springer-Verlag New York, Inc., New York, NY, USA, 1997.

[19] C.-K. Shene. CS3621 Introduction to Computing with Geometry. http://www.cs.mtu.edu/~shene/COURSES/cs3621/NOTES/, July 2011.

[20] J. Lowther J. Fisher and C.-K. Shene. If you know B-Splines well, you also know NURBS! *SIGCSE Bull.*, 36:343–347, March 2004.

[21] M. G. Cox. The numerical evaluation of B-splines. Technical report, National Physics Laboratory DNAC 4, 1971.

[22] C. De Boor. On calculation with B-splines. *Journal of Approximation Theory*, 6:50–62, 1972.

[23] X. Tu and J. E. Andrade. Criteria for static equilibrium in particulate mechanics computations. *International Journal for Numerical Methods in Engineering*, 75:1581–1606, 2008.

[24] R. Hart, P. A. Cundall, and J. Lemos. Formulation of a three-dimensional distinct element model - Part II: Mechanical calculations for motion and interaction of a system composed of many polyhedral blocks. *International Journal of Rock Mechanics and Mining Sciences*, 25(3):117–125, 1988.

[25] C. Hogue and D. Newland. Efficient computer simulation of moving granular particles. *Powder Technology*, 78(1):51 – 66, 1994.

[26] A. Džiugys and B. Peters. An approach to simulate the motion of spherical and non-spherical fuel particles in combustion chambers. *Granular Matter*, 3(4):231–266, 2001.

[27] A. M. Sallam. *Studies on Modeling Angular Soil Particles Using the Discrete Element Method*. PhD thesis, University of South Florida, Tampa, FL, 2004.

[28] Knut Mørken, Martin Reimers, and Christian Schulz. Computing intersections of planar spline curves using knot insertion. *Comput. Aided Geom. Des.*, 26:351–366, March 2009.

[29] T. Dokken. Finding intersections of B-spline represented geometries using recursive subdivision techniques. *Computer Aided Geometric Design*, 2(1-3):189–195, September 1985.

[30] SINTEF ICT, Department of Applied Mathematics, Norway. The SINTEF Spline Library. http://www.sintef.no/sisl.

[31] T. W. Sederberg and T. Nishita. Curve intersection using Bézier clipping. *Comput. Aided Des.*, 22:538–549, 1990.

[32] Christian Schulz. Bézier clipping is quadratically convergent. *Computer Aided Geometric Design*, 26(1):61 – 74, 2009.

[33] A. Krishnamurthy, R. Khardekar, S. McMains, K. Haller, and G. Elber. Performing efficient NURBS modeling operations on the GPU. In *Proceedings of the 2008 ACM Symposium on Solid and Physical Modeling*, SPM '08, pages 257–268. ACM, 2008.

[34] M. Babić. Discrete Particle Numerical Simulation of Granular Material Behavior. Technical Report 88-11, Department of Civil and Environmental Engineering, Clarkson University, 1988.

[35] R. D. Mindlin. Compliance of elastic bodies in contact. *Journal of Applied Mechanics*, 71:259–268, 1949.

[36] J. E. Andrade, C. F. Avila, N. Lenoir, S. A. Hall, and G. Viggiani. Multiscale modeling and characterization of granular matter: from grain scale kinematics to continuum mechanics. *Journal of the Mechanics and Physics of Solids*, 59:237–250, 2011.

[37] J. E. Andrade and C. F. Avila. Granular element method (GEM): linking inter-particle forces with macroscopic loading. *Granular Matter*, 14:1–13, 2012.